Research Square

Preprints are preliminary reports that have not undergone peer review.
They should not be considered conclusive, used to inform clinical practice,
or referenced by the media as validated information.

A native-state chemical atlas of the aging osteochondral interface

Wenguo Cui

wgcui80@hotmail.com

Shanghai Jiao Tong University School of Medicine

Jie Chen

Shanghai Jiao Tong University School of Medicine

Baikun Liu

Shanghai Jiao Tong University School of Medicine

Jiawei Chen

Shanghai Jiao Tong University School of Medicine

Ke Yang

Shanghai Jiao Tong University School of Medicine

Huitong Ruan

Ruijin Hospital, Shanghai Jiao Tong University School of Medicine https://orcid.org/0000-0002-5200-8149

Yuchen Liu

Shanghai Jiao Tong University School of Medicine

Lu Luo

Shanghai Jiao Tong University School of Medicine

Xiaoyu Zhao

Supervision Medicine Co., Ltd, Xiang Hu Lab

Article

Keywords: Spatial chemical omics, Label-free Raman imaging, Osteochondral aging, Native mineralized tissue, Aging atlas

Posted Date: August 11th, 2026

DOI: https://doi.org/10.21203/rs.3.rs-10339369/v1

License: This work is licensed under a Creative Commons Attribution 4.0 International License.
Read Full License

Additional Declarations: There is **NO** Competing Interest.

A native-state chemical atlas of the aging osteochondral interface

Jie Chen[1#], Baikun Liu[1#], Jiawei Chen[2], Ke Yang[2], Huitong Ruan[1], Yuchen Liu[1], Lu Luo[1], Xiaoyu Zhao[3]*, Wenguo Cui[1]*

[1]Department of Orthopaedics, Shanghai Key Laboratory for Prevention and Treatment of Bone and Joint Diseases, Shanghai Institute of Traumatology and Orthopaedics, Ruijin Hospital, Shanghai Jiao Tong University School of Medicine, 197 Ruijin 2nd Road, Shanghai, 200025, PR China.

[2]Department of Cardiovascular Medicine, Ruijin Hospital, Shanghai Jiaotong University School of Medicine, No. 197 Ruijin Second Rd, Shanghai 200025, China.

[3]Supervision Medicine Co., Ltd, Xiang Hu Lab, Hangzhou, Zhejiang, 311215, China.

*Corresponding authors: Xiaoyu Zhao (xiaoyuzhao@supervisionmedicine.tech), Wenguo Cui (wgcui@sjtu.edu.cn)

[#] Contributed equally to this work: J.C., B. L.

Abstract

Age-associated osteoarticular degeneration is thought to arise from coordinated failure of the osteochondral unit, but its native chemical organization remains poorly defined. This gap reflects the difficulty of preserving hydration, mineral phases and labile metabolites while resolving molecular heterogeneity across cartilage and subchondral bone. Here we develop Panoramic Biomolecular Imaging in Pristine Samples (PBI-PS), a label-free Raman-based approach for fresh, unfixed and undecalcified osteochondral tissue. PBI-PS maps approximately 70 biochemical signatures at ~800 nm resolution within a shared spatial frame. Applied to mouse joints during aging, this approach reveals an interface-centred chemical programme linking proteoglycan and water loss, collagen and hydroxyapatite accumulation, metabolic remodeling, inflammatory and senescence-associated niche formation, and attenuation of repair-associated progenitor signals. These data suggest that osteochondral aging is organized by spatially coupled chemical states at the cartilage–bone interface, rather than by independent degeneration of cartilage and bone. PBI-PS provides a native-state framework for interrogating mineralized tissues.

Keywords: Spatial chemical omics; Label-free Raman imaging; Osteochondral aging; Native mineralized tissue; Aging atlas

Introduction

Musculoskeletal aging is a major cause of pain, reduced mobility, frailty and loss of healthspan in older adults. Degenerative osteoarticular disorders, including osteoarthritis (OA) and osteoporosis (OP), are increasing with population aging and impose a growing clinical and socioeconomic burden [1]. Although OA and OP are often described by their dominant tissue phenotypes, such as cartilage degeneration or bone loss, the aging joint is not a collection of isolated compartments. Cartilage, calcified cartilage and subchondral bone form an integrated osteochondral unit in which matrix composition, mineral homeostasis, tissue hydration, mechanical loading, cellular state and metabolism are tightly connected [2-5]. Understanding how these components change together is therefore essential for defining the biology of osteoarticular aging.

The cartilage–bone interface is a key site at which this coupling may be organized. This spatially confined transition zone links soft, hydrated cartilage to mineralized subchondral bone and contains steep gradients in extracellular matrix organization, mineral content, water distribution, cell-associated signals and metabolic activity [2-5]. Age-related degeneration is therefore unlikely to proceed only as a sequential loss of cartilage followed by bone remodeling, or as independent deterioration of separate tissues. Instead, the osteochondral interface may act as a chemical and biological hub through which matrix damage, mineral expansion, inflammatory signaling, metabolic stress and niche dysfunction become spatially coordinated. How such multi-component remodeling emerges and propagates across the native interface remains unresolved.

Progress has been limited by the difficulty of measuring diverse biochemical states in intact mineralized tissues. Single-cell and spatial transcriptomic approaches have transformed the study of cellular programs, and spatial proteomic, metabolomic and mass-spectrometry imaging methods have expanded molecular mapping in tissues [6-9]. However, many of these technologies are optimized for selected molecular layers and are not designed to capture organic matrix molecules, inorganic mineral phases, water and small metabolites within the same spatial framework [6-8]. This limitation is particularly important in osteochondral tissues, where hydration and mineral organization are central to function. Standard preparation procedures, including fixation, decalcification, dehydration, solvent exposure and section processing, can alter soluble metabolites, disrupt water-dependent chemistry and remove or distort mineralized compartments [7,9,10]. Dense calcified cartilage and subchondral bone also reduce molecular accessibility, leaving the interface incompletely characterized.

Raman spectroscopy provides a label-free, bond-specific chemical readout and is well suited for detecting both organic and inorganic components in situ [11-14]. These features make it attractive for native-state analysis of hydrated and mineralized tissues. Yet comprehensive Raman imaging of the osteochondral interface remains technically challenging. Conventional systems often face limited spectral coverage, weak signals from low-abundance molecular species, reduced signal-to-noise at depth and strong scattering in mineralized matrices [14-17]. Large-area imaging of fresh tissues also requires

a balance between spectral sensitivity, spatial resolution and photothermal damage [18-20]. As a result, current Raman-based approaches have not fully enabled high-dimensional, same-site biochemical mapping of intact osteochondral aging.

Here we introduce Panoramic Biomolecular Imaging in Pristine Samples (PBI-PS), a full-spectrum Raman-based framework for spatially co-registered chemical imaging of fresh, unfixed and undecalcified osteochondral tissue. PBI-PS combines low-damage spectral acquisition, water-immersion optics, volumetric confocal imaging and reference-guided spectral unmixing to map approximately 70 molecular signatures within a shared native tissue space. Using mouse joints across aging, we generate a chemical atlas of the osteochondral unit and show that aging is accompanied by coordinated remodeling of proteoglycans, collagen I, hydroxyapatite, water, metabolic intermediates, lipids, amino acids, oxidative stress-associated molecules, inflammatory mediators and stem/progenitor-associated microenvironments. Correlation and predictor analyses reveal progressive rewiring of matrix–mineral–metabolic relationships at the cartilage–bone interface. These data support a model in which osteochondral aging is organized by interface-centred chemical coupling rather than by a linear, tissue-restricted degenerative cascade.

Results

PBI-PS enables native-state spatial chemical imaging of the osteochondral interface

To resolve the biochemical organization of intact mineralized tissues under native conditions, we developed Panoramic Biomolecular Imaging in Pristine Samples (PBI-PS), a label-free Raman-based imaging framework for fresh, unfixed and undecalcified osteochondral tissue. PBI-PS integrates native sample preservation, low-damage confocal Raman acquisition, water-immersion optics and reference-guided spectral unmixing to capture extracellular matrix components, mineral phases, water, metabolites, lipids and niche-associated biochemical signatures within the same spatial coordinate system (**Fig. 1a, b**).

The spectral unmixing strategy decomposes each pixel spectrum into a linear combination of reference biochemical signatures, allowing overlapping Raman signals to be assigned to annotated molecular classes, including proteins, proteoglycans, mineral components, lipids, metabolites and cell-associated states (**Extended Data Fig. 1a, b**). A curated spectral reference library supported the assignment of approximately 70 biochemical signatures. Volumetric spectral acquisition further enabled three-dimensional reconstruction of the osteochondral biochemical landscape without fixation, decalcification or cross-platform image registration (**Extended Data Fig. 1c**).

PBI-PS resolved spatially ordered molecular gradients across the osteochondral interface. Aggrecan-rich proteoglycan signals were enriched in hyaline cartilage, whereas collagen I and hydroxyapatite signals increased toward calcified cartilage and subchondral bone. Water, unsaturated lipid and BMSC-associated signatures further delineated local biochemical microenvironments across the interface (**Fig. 1c–e**). Quantitative analysis confirmed age-associated changes in aggrecan, collagen I, hydroxyapatite, unsaturated lipids, water and BMSC-associated signals, indicating that these components represent major biochemical axes of the osteochondral interface (**Fig. 1e**). Raman-defined tissue boundaries were consistent with Safranin O–Fast Green staining, supporting preservation of tissue morphology and spatial organization (**Fig. 1f**). Together, these data establish PBI-PS as a native-state spatial chemical omics platform for high-dimensional imaging of intact osteochondral tissue (**Fig. 1g**).

Matrix loss and mineral expansion mark structural remodeling of the aging osteochondral interface

We next applied PBI-PS to mouse joints at young, adult and old ages to examine how the osteochondral interface is remodeled during aging. Histological analysis showed progressive cartilage thinning, tidemark advancement and expansion of mineralized tissue into the cartilage–bone interface (**Fig. 2a**). These changes were not restricted to the articular surface but extended across the osteochondral transition zone, suggesting that degeneration progresses through the interface.

Native biochemical maps revealed a reciprocal transition between cartilage-like and

bone-like matrix states. Cartilage-associated components, including aggrecan, hyaluronan and versican V0, declined with age, whereas collagen I and hydroxyapatite expanded toward the interface and cartilage regions (**Fig. 2b, f**). This pattern indicates a shift from a proteoglycan-rich, hydrated cartilage matrix toward a collagen I- and mineral-rich tissue state.

Osteogenic and remodeling-associated signals showed a similar spatial progression. RUNX2, BMP2 and SPP1 increased with age and localized to regions of matrix disruption and mineral advance (**Fig. 2c, f**). Multiplex immunofluorescence confirmed the accumulation of collagen I, BMP2, RUNX2 and SPP1 in the aging interface and subchondral compartment (**Fig. 2d, e**). Extended matrix profiling further showed coordinated changes in fibronectin, laminin, vitronectin, syndecan, RANKL, tenascin C and vimentin, consistent with broader extracellular matrix remodeling and fibrosis-like reorganization of the interface (**Extended Data Fig. 2**). Thus, osteochondral aging is marked by a structural axis in which proteoglycan loss, collagen I accumulation and mineral expansion occur as a spatially coordinated process.

Metabolic remodeling spatially coincides with matrix degeneration

We then asked whether matrix and mineral remodeling were accompanied by local metabolic changes. Within the same imaging coordinates, regions with preserved aggrecan showed relatively stable metabolic patterns, whereas regions with proteoglycan loss and mineral expansion accumulated glycolysis-associated signatures, including lactate, glucose-6-phosphate-related signals and sodium pyruvate (**Fig. 3a**). This spatial relationship links matrix destabilization to a shift in local energy metabolism.

Additional metabolic signatures also changed with age. NAD, TAG-related lipid signals, cholesterol esters, α-ketoglutarate-related signatures and L-alanine were redistributed across the aging interface, suggesting changes in redox balance, mitochondrial metabolism, lipid handling and amino acid metabolism (**Fig. 3b–d**). Lipid remodeling was particularly prominent, with increased unsaturated lipid and cholesterol ester signals and localized enrichment of arachidonic acid-related signatures, indicating activation of inflammatory lipid-associated pathways (**Extended Data Fig. 3**).

Orthogonal metabolomic analysis supported the Raman-derived metabolic patterns. Glycolipid profiles showed age-dependent stratification, and selected metabolites recapitulated the spatial and quantitative trends observed by PBI-PS (**Fig. 3e, f**). Broader profiling further identified coordinated changes in fatty acid metabolism, pyruvate-related pathways, redox cofactors and amino acid metabolism (**Extended Data Figs. 3–5**). These findings indicate that metabolic remodeling is not a secondary diffuse change but is spatially coupled to structural degeneration at the cartilage–bone interface.

Aging is associated with an inflammatory and senescence-related interface state

We next examined whether structural and metabolic remodeling was accompanied by changes in senescence-, inflammatory- and repair-associated biochemical signatures. PBI-PS detected age-associated increases in CDKN1A- and CDKN2A-associated signals, together with IL-6-, IL-11- and TNF-α-associated signatures, particularly at the osteochondral interface and subchondral regions (**Fig. 4a, f**). In contrast, IGF-1-, PDGF-AA- and Noggin-associated signals were reduced with age (**Fig. 4b, f**). This reciprocal pattern suggests a shift from a repair-supportive biochemical environment toward a stress- and inflammation-associated interface state.

Multiplex immunofluorescence supported the spatial enrichment of p16/p21-related senescence markers and inflammatory signals in regions of matrix disruption and subchondral remodeling (**Fig. 4c–e**). These changes were not uniformly distributed across the joint, but were concentrated around the cartilage–bone interface, indicating that inflammatory and senescence-related features are spatially linked to structural deterioration.

Extended profiling further identified age-associated increases in oxidative and carbonyl stress-related signatures, including 8-OHdG, 3-nitrotyrosine, 4-hydroxynonenal, CEL and propanedial, together with immune-related signals such as M-CSF, CD68, C3, STING, CD98, IL-12 and IL-2 (**Extended Data Figs. 6, 7**). Protective or antioxidant-associated signals, including SOD and A20, were reduced. These data indicate that osteochondral aging is accompanied by a local imbalance between damage-associated biochemical stress and repair-associated signals at the interface.

Integrative modeling identifies an interface-centred chemical aging signature

To determine whether the multidimensional biochemical changes detected by PBI-PS converged into a coherent age-associated pattern, we constructed an integrative modeling pipeline using the high-dimensional Raman dataset (**Fig. 5a**). We first defined interface anchor states, including water, BMSC-associated signatures, hydroxyapatite, collagen I and hyaluronan, to represent the native physicochemical organization of the osteochondral interface. Relative to these anchor states, hydroxyapatite, unsaturated lipids, lactate, L-alanine, NAD and IL-11-associated signals emerged as a compact age-associated chemical signature linking matrix composition, mineralization, metabolism and inflammatory signaling (**Fig. 5b**).

Principal component analysis separated young, adult and old samples, indicating that aging is accompanied by coordinated chemical drift across the interface (**Fig. 5c**). LASSO regression further reduced the high-dimensional feature space to a sparse predictor set spanning mineral composition, lipid remodeling, redox state, amino acid metabolism and inflammatory signaling (**Fig. 5d**). Trajectory analysis showed that 71.8% of quantified variables followed non-linear age-associated changes, with major shifts detectable between young and adult stages and a more consolidated profile in old tissue (**Fig. 5e**). This pattern suggests that substantial biochemical remodeling of the osteochondral interface precedes or accompanies late-stage tissue degeneration.

Correlation and network analyses showed that these age-associated variables were not independent. Instead, they formed a coupled chemical network around interface anchor states, linking hydroxyapatite, collagen I, hyaluronan, water, BMSC-associated signatures, lactate, NAD, IL-11-associated signals, L-alanine and unsaturated lipids (**Fig. 5f**). These findings identify an interface-centred chemical aging signature that integrates structural, metabolic and inflammatory dimensions of osteochondral aging.

Discussion

Here we establish a native-state spatial chemical atlas of osteochondral aging and show that age-associated degeneration is organized around the cartilage–bone interface. By imaging fresh, unfixed and undecalcified osteochondral tissue, PBI-PS resolves extracellular matrix composition, mineral phases, water, metabolic signatures and niche-associated biochemical states within the same tissue space. Our data indicate that matrix loss, mineral expansion, metabolic remodeling, oxidative stress, inflammatory and senescence-associated signatures, and reduced repair-associated signals emerge in a spatially coordinated pattern at the osteochondral interface. These findings support a model in which osteochondral aging is accompanied by interface-centered biochemical remodeling, rather than by isolated or strictly sequential changes in cartilage and bone.

This interface-centered view is important because cartilage and subchondral bone are often studied as separate compartments, despite their close structural and functional connection. The osteochondral interface links a soft, proteoglycan-rich and hydrated cartilage matrix to a mineralized subchondral compartment. This transition zone is therefore well positioned to integrate mechanical, metabolic and biochemical stress during aging. In our study, proteoglycan and water loss occurred alongside collagen I accumulation, hydroxyapatite expansion and remodeling-associated signals. These structural changes were spatially associated with altered glycolytic, lipid, redox and amino acid-related signatures, suggesting that matrix and metabolic states change together within the aging interface. Although these observations do not establish causal relationships, they reveal a shared spatial context in which structural degeneration and biochemical remodeling converge.

Our results also show that osteochondral aging is accompanied by a shift in the local biochemical niche. Senescence-associated and inflammation-associated signals, including CDKN1A-, CDKN2A-, IL-6-, IL-11- and TNF-α-related signatures, were enriched in regions of matrix disruption and subchondral remodeling. In parallel, repair- and trophic-associated signals, including IGF-1, PDGF-AA and Noggin, were reduced. Additional increases in oxidative and carbonyl stress-associated signatures further suggest that the aging interface is characterized by an imbalance between damage-related biochemical stress and repair-associated activity. These findings do not indicate that any single pathway initiates osteochondral degeneration. Rather, they identify an interface-associated tissue state in which matrix remodeling, mineralization, metabolic stress and inflammatory features are spatially linked.

This perspective extends previous models of osteochondral degeneration. Earlier

studies have shown that cartilage damage, subchondral bone remodeling and metabolic dysregulation are closely related during osteoarthritis and musculoskeletal aging [4,5,21,22]. However, many of these studies relied on histology, bulk molecular profiling or spatial methods that require tissue fixation, decalcification or molecular extraction. Such approaches have limited ability to preserve water-dependent chemistry, mineral organization and soluble biochemical states in the same native tissue space [9,109,10]. By contrast, PBI-PS enables direct in situ visualization of multiple chemical classes in fresh, undecalcified osteochondral tissue. This allows matrix, mineral, metabolic and niche-associated features to be examined together, without cross-platform registration or extensive sample processing.

From a methodological standpoint, the main advance of PBI-PS lies in combining native tissue preservation with high-dimensional Raman-based chemical imaging. Raman spectroscopy is well suited to mineralized tissues because it can detect both organic and inorganic components without labeling [11,13,14,18]. However, large-area imaging of fresh hard tissue has been limited by weak signals, scattering, spectral overlap and the need to avoid photothermal damage [12,14-20]. By integrating low-damage spectral acquisition, water-immersion optics, volumetric confocal imaging and reference-guided spectral unmixing, PBI-PS provides voxel-resolved chemical phenotyping of the osteochondral interface while preserving hydration and mineral integrity. This approach complements existing spatial transcriptomic, proteomic and metabolomic methods by providing a native-state chemical layer that is especially suited to complex mineralized tissue [6-8].

The integrative modeling further suggests that osteochondral aging can be represented by a compact chemical signature. Hydroxyapatite, unsaturated lipids, lactate, L-alanine, NAD and IL-11-associated signals emerged as age-associated features linking mineral expansion, lipid remodeling, metabolic state and inflammatory signaling. Principal component, regression and network analyses indicated that these features were not independent but were connected to interface anchor states such as water, collagen I, hyaluronan, hydroxyapatite and BMSC-associated signatures. These analyses should be interpreted as evidence of coordinated age-associated organization, not proof of direct molecular causality. Nevertheless, they provide a focused set of candidate features and spatial relationships for future mechanistic testing.

Several limitations should be considered. First, the present atlas was generated from mouse osteochondral tissues, and validation in human samples will be needed to determine how these patterns relate to human aging, osteoarthritis and osteoporotic joint changes. Second, although spectral unmixing enables high-dimensional chemical annotation, detection of low-abundance or highly overlapping components depends on the completeness of the reference library and the assumptions of the chemometric model. Orthogonal validation remains important for key low-abundance cytokine-, senescence- and niche-associated signals. Third, the current study defines spatially coordinated biochemical states but does not establish causal mechanisms. Functional perturbation studies, longitudinal models, cell-type-specific validation and integration

with complementary omics will be required to determine whether matrix remodeling, mineral expansion, metabolic stress and inflammatory signaling actively regulate one another during osteochondral aging.

In summary, PBI-PS provides a native-state spatial chemical atlas of the aging osteochondral interface. The data show that age-associated degeneration is accompanied by coordinated remodeling of matrix, mineral, metabolic, oxidative stress, inflammatory and repair-associated biochemical states within a shared tissue space. This work supports an interface-centered model of osteochondral aging and provides a framework for mapping complex mineralized tissues without fixation or decalcification. More broadly, native-state chemical imaging may help define early tissue states, identify spatially organized disease signatures and guide future mechanistic studies of age-related osteoarticular disease.

Acknowledgements

J.C., and B.L. contributed equally to this work. This work was supported by the Noncommunicable Chronic Diseases-National Science and Technology Major Project (2023ZD0500700), the National Natural Science Foundation of China (52273133, 52305206, 82501061).

Author contributions

J.C., B.L., and W.C. designed and conceived this research. J.C., B.L., Y.L., L.L., and Y.L. prepared the animal samples, made sections, and performed immunofluorescence staining. J.C., B.L., N.W., and J.C. analyzed and interpreted the data. J.C., B.L., H.L., and H. R. prepared the figures and drafted the manuscript. K.Y., H. R., T.Y, and W.C. revised the manuscript. All authors approved the final version of the manuscript.

Declaration of interests

The authors declare no competing interests.

Ethical approval

All animal experiments were approved by the Institutional Animal Care and Use Committee (approval no. 2026-01-RJYY-CJ-134).

Figure legends

Fig. 1 | PBI-PS enables native-state spatial chemical imaging of the osteochondral interface.

a, Schematic of the PBI-PS platform integrating volumetric confocal Raman acquisition with full-spectrum spectral unmixing, enabling label-free, in situ biochemical profiling of intact osteochondral tissue without decalcification or fixation.

b, Imaging workflow for fresh, native specimens, establishing a shared spatial coordinate system that allows direct cross-component comparison at single-pixel resolution across cartilage, calcified cartilage, and subchondral bone.

c, Representative multicomponent maps across ages showing spatial distributions of extracellular matrix (AGC), fibrotic matrix (COL I), mineral (HAp), lipids (UL), water, and BMSC-associated signals, which were defined based on Raman spectral features corresponding to previously annotated stem-cell–related biochemical signatures, revealing a continuous biochemical gradient across the osteochondral interface.

d, Interface-resolved views demonstrate that age-dependent remodeling is concentrated at the cartilage–bone boundary, characterized by coordinated AGC depletion and COL I expansion.

e, Quantitative analysis confirms synchronized shifts in matrix composition, mineral deposition, metabolic features, and niche-associated biochemical signals, indicating coordinated biochemical remodeling across multiple molecular layers.

f, Raman-defined compartmentalization aligns with histological boundaries, validating structural fidelity while preserving native biochemical information.

g, Data architecture illustrating simultaneous extraction of ~70 biochemical components at ~800 nm spatial resolution, establishing a high-dimensional, shared spatial coordinate system biochemical atlas of osteochondral tissue.

Fig. 2 | Matrix loss and mineral expansion mark structural remodeling of the aging osteochondral interface.

a, Histology reveals progressive cartilage thinning, tidemark elevation, and subchondral bone encroachment, indicating that degeneration propagates inward from the interface rather than remaining superficial.

b, Raman maps show depletion of cartilage ECM components (Aggrecan, Hyaluronan, Versican V0) alongside expansion of Collagen1 and Hydroxyapatite, demonstrating replacement of cartilage-like matrix by bone-like and mineralized tissue.

c, Osteogenic regulators (RUNX2, BMP2, SPP1) accumulate specifically at the advancing interface front, consistent with active osteogenic remodeling at the advancing interface.

d-e, Immunofluorescence confirms expansion of bone/osteogenic programs (COL I,

BMP2, RUNX2, and SPP1), validating age-dependent activation of osteogenic programs in the osteochondral interface and subchondral compartment.

f, Quantification shows a coordinated shift from cartilage-associated to bone-associated molecular states.

Fig. 3 | Metabolic remodeling spatially coincides with matrix degeneration.

a, A shared spatial coordinate system mapping shows that regions with preserved Aggrecan maintain baseline metabolic profiles, whereas matrix erosion zones accumulate glycolytic intermediates (Lactate, G6P-Na, Sodium Pyruvate), indicating localized metabolic activation.

b, Spatial anti-correlation between Aggrecan and Lactate demonstrates that matrix destabilization and glycolytic activation are tightly coupled processes.

c, Additional maps reveal concurrent reorganization of redox and lipid metabolism (NAD, TAGmix, Cholesterol ester, L-Alanine), indicating coordinated changes in redox and lipid metabolism.

d, Quantification confirms coordinated elevation of glycolytic, lipid, and redox-associated metabolites during degeneration.

e-f, External metabolomics independently validates age-dependent stratification and confirms key metabolic trends observed in situ.

Fig. 4 | Aging is associated with an inflammatory and senescence-related interface state.

a, Raman maps show accumulation of senescence markers (CDKN1A, CDKN2A) and inflammatory cytokines (IL-6, IL-11, TNF-α), spatially concentrated at the interface and expanding with age.

b, In contrast, trophic and homeostatic factors (IGF-1, PDGF-AA, Noggin) progressively decline, consistent with reduced trophic support.

c-e, Immunofluorescence confirms localized enrichment of senescence (P16, P21) and inflammatory signalling (IL-6, IL-2, TNF-α), forming dense clusters near the interface in aged tissue.

f, Quantification demonstrates a coordinated shift from a trophic to a pro-inflammatory niche state.

Fig. 5 | Integrative modeling identifies an interface-centred chemical aging signature.

a, Workflow illustrating the integrative chemometric pipeline combining spatially resolved Raman features with multivariate modelling to define system-level organization across the osteochondral interface.

b, Feature selection defining interface homeostatic anchor states (Water, BMSC-

associated signals, Hydroxyapatite (HAp), Collagen I (COL I), and Hyaluronan (HA)) and key aging-associated variables (HAp, Unsaturated Lipid (UL), Lactate, L-Alanine, NAD, and IL-11), spanning matrix composition, metabolism, and inflammatory signalling.

c, Principal component analysis (PCA) showing clear separation of samples by age, indicating coordinated system-level variation across the osteochondral unit.

d, LASSO regression identifying a reduced set of predictive features from the high-dimensional dataset, integrating matrix, lipid, amino acid, and inflammatory pathways.

e, Temporal trajectory analysis of selected variables, showing that the majority (71.8%) exhibit non-linear transitions, with major shifts occurring between early and mid-life stages and relative stabilization in aged tissue.

f, Correlation-based network analysis demonstrating strong coupling between predictive variables and interface anchor states, forming an interface-centred molecular network linking mineralization, hydration, extracellular matrix organization, metabolism, and inflammatory signalling.

Reference

1 GBD 2021 Osteoarthritis Collaborators. Global, regional, and national burden of osteoarthritis, 1990-2020 and projections to 2050: a systematic analysis for the Global Burden of Disease Study 2021. *The Lancet. Rheumatology* **5**, e508-e522 (2023).

2 Hu, Y. J. *et al.* Mechanical and structural properties of articular cartilage and subchondral bone in human osteoarthritic knees. *Journal of Bone Mineral Research* **39**, 1120-1131 (2024).

3 Fan, X., Wu, X., Crawford, R., Xiao, Y. & Prasadam, I. J. Macro, micro, and molecular. Changes of the osteochondral interface in osteoarthritis development. *Frontiers in Cell Developmental Biology* **9**, 659654 (2021).

4 Goldring, S. R. & Goldring, M. B. Changes in the osteochondral unit during osteoarthritis: structure, function and cartilage–bone crosstalk. *Nature Reviews Rheumatology* **12**, 632-644 (2016).

5 Findlay, D. M. & Kuliwaba, J. S. Bone–cartilage crosstalk: a conversation for understanding osteoarthritis. *Bone research* **4**, 16028 (2016).

6 Frangieh, C. J. *et al.* Single-cell and spatial profiling in cancer biology and clinical oncology. *Nature Cancer*, 1-11 (2026).

7 Liu, L. *et al.* Spatiotemporal omics for biology and medicine. *Cell* **187**, 4488-4519 (2024).

8 Ståhl, P. L. *et al.* Visualization and analysis of gene expression in tissue sections by spatial transcriptomics. *Science (New York, N.Y.)* **353**, 78-82 (2016).

9 Good, C. J. *et al.* High spatial resolution MALDI imaging mass spectrometry of fresh-frozen bone. *Analytical Chemistry* **94**, 3165-3172 (2022).

10 Hosoya, A. *et al.* Effects of fixation and decalcification on the immunohistochemical localization of bone matrix proteins in fresh-frozen bone sections. *Histochemistry and Cell Biology* **123**, 639-646 (2005).

11 Freudiger, C. W. *et al.* Label-free biomedical imaging with high sensitivity by stimulated Raman scattering microscopy. *Science (New York, N.Y.)* **322**, 1857-1861 (2008).

12 Guo, J. *et al.* Super-broadband stimulated Raman scattering spectroscopy and imaging. *Nature Photonics*, 1-8 (2026).

13 Cheng, J.-X. & Xie, X. S. Vibrational spectroscopic imaging of living systems: An emerging platform for biology and medicine. *Science (New York, N.Y.)* **350**, aaa8870 (2015).

14 Unal, M., Ahmed, R., Mahadevan-Jansen, A. & Nyman, J. S. Compositional assessment of bone by Raman spectroscopy. *Analyst* **146**, 7464-7490 (2021).

15 Camp J. *et al.* High-speed coherent Raman fingerprint imaging of biological tissues. *Nature Photonics* **8**, 627-634 (2014).

16 Wei, L. *et al.* Super-multiplex vibrational imaging. *Nature* **544**, 465-470 (2017).

17 Matousek, P. & Stone, N. J. Development of deep subsurface Raman spectroscopy for medical diagnosis and disease monitoring. *Chemical Society Reviews* **45**, 1794-1802 (2016).

18 Schulmerich, M. V. *et al.* Transcutaneous Raman spectroscopy of murine bone in vivo. *Applied Spectroscopy* **63**, 286-295 (2009).

19 Wang, Y., Fang, L., Wang, Y. & Xiong, Z. J. Current trends of Raman spectroscopy in clinic settings: opportunities and challenges. *Advanced Science* **11**, 2300668 (2024).

20 Min, W., Cheng, J.-X. & Ozeki, Y. J. Theory, innovations and applications of stimulated Raman scattering microscopy. *Nature Photonics* **19**, 803-816 (2025).

21 Hu, Y., Chen, X., Wang, S., Jing, Y. & Su, J. Subchondral bone microenvironment in osteoarthritis and pain. *Bone research* **9**, 20 (2021).

22 Collins, K. H., Haugen, I. K., Neogi, T. & Guilak, F. Osteoarthritis as a systemic disease. *Nature Reviews Rheumatology* **22**, 105-117 (2026).

23 Liu, X. *et al.* A decoupling strategy toward spatiotemporal regulation and biomechanical transmission of sandwiched scaffold for osteochondral regeneration.

Nature communications **17**, 5351 (2026).
24 Mella, M., Schweitzer, B., Mallet, C. R., Moore, T. & Botch-Jones, S. J. Detection of cocaine and metabolites in bone following decomposition using 2D LC–MS-MS. *Journal of Analytical Toxicology* **42**, 265-275 (2018).
25 Chong, J., Yamamoto, M. & Xia, J. J. M. MetaboAnalystR 2.0: from raw spectra to biological insights. *Metabolites* **9**, 57 (2019).
26 Friedman, J. H., Hastie, T. & Tibshirani, R. J. Regularization paths for generalized linear models via coordinate descent. *Journal of Statistical Software* **33**, 1-22 (2010).

Fig. 1

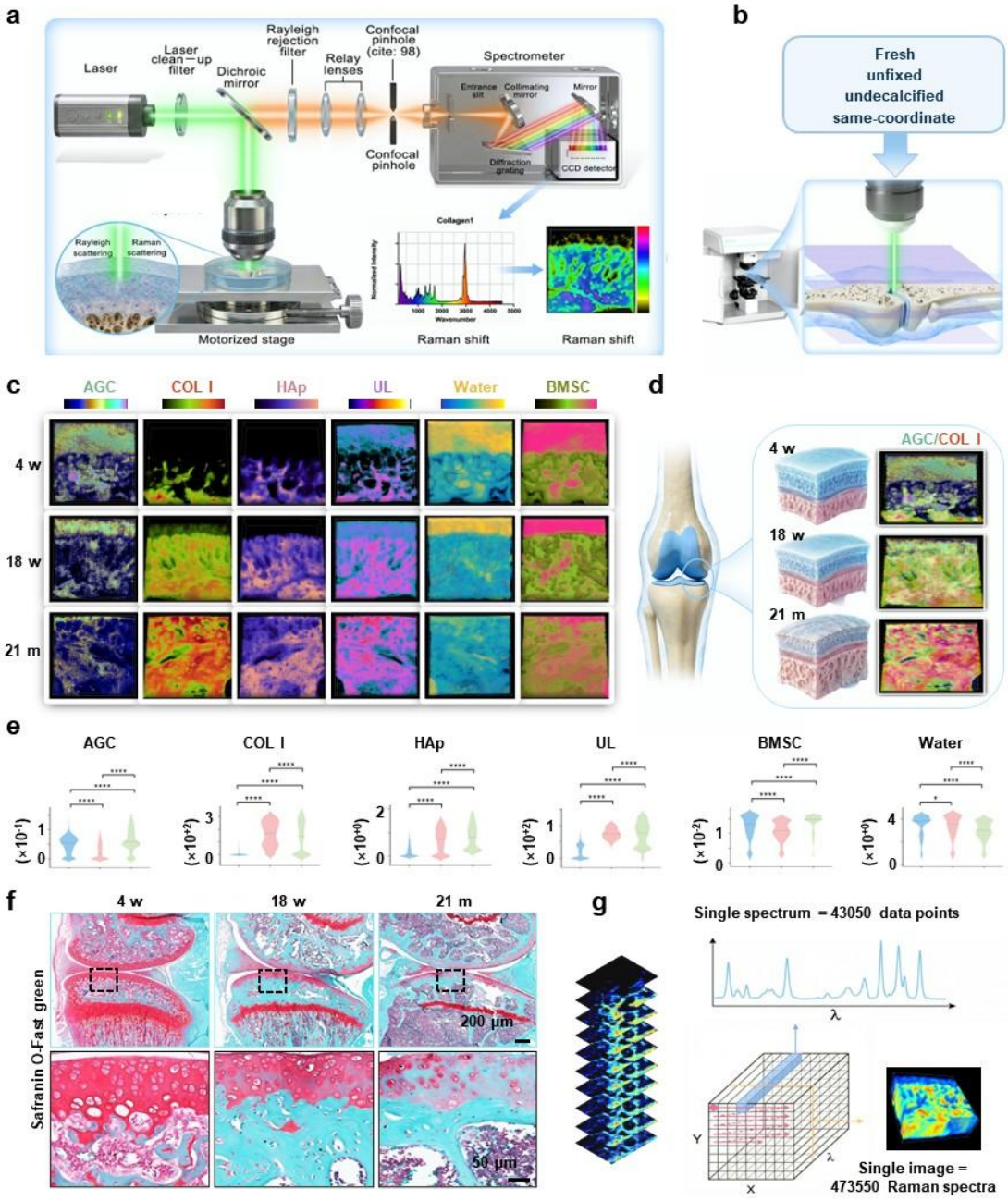

a
Laser
Laser clean−up filter
Dichroic mirror
Rayleigh rejection filter
Relay lenses
Confocal pinhole (cite: 98)
Confocal pinhole
Spectrometer
Entrance slit
Collimating mirror
Mirror
Diffraction grating
CCD detector
Rayleigh scattering
Raman scattering
Motorized stage
Collagen1
Raman shift
Raman shift
b
Fresh
unfixed
undecalcified
same-coordinate
c
AGC
COL I
HAp
UL
Water
BMSC
4 w
18 w
21 m
d
AGC/COL I
4 w
18 w
21 m
e
AGC
COL I
HAp
UL
BMSC
Water
f
4 w
18 w
21 m
Safranin O-Fast green
200 μm
50 μm
g
Single spectrum = 43050 data points
λ
Y
x
Single image =
473550 Raman spectra

Fig. 2

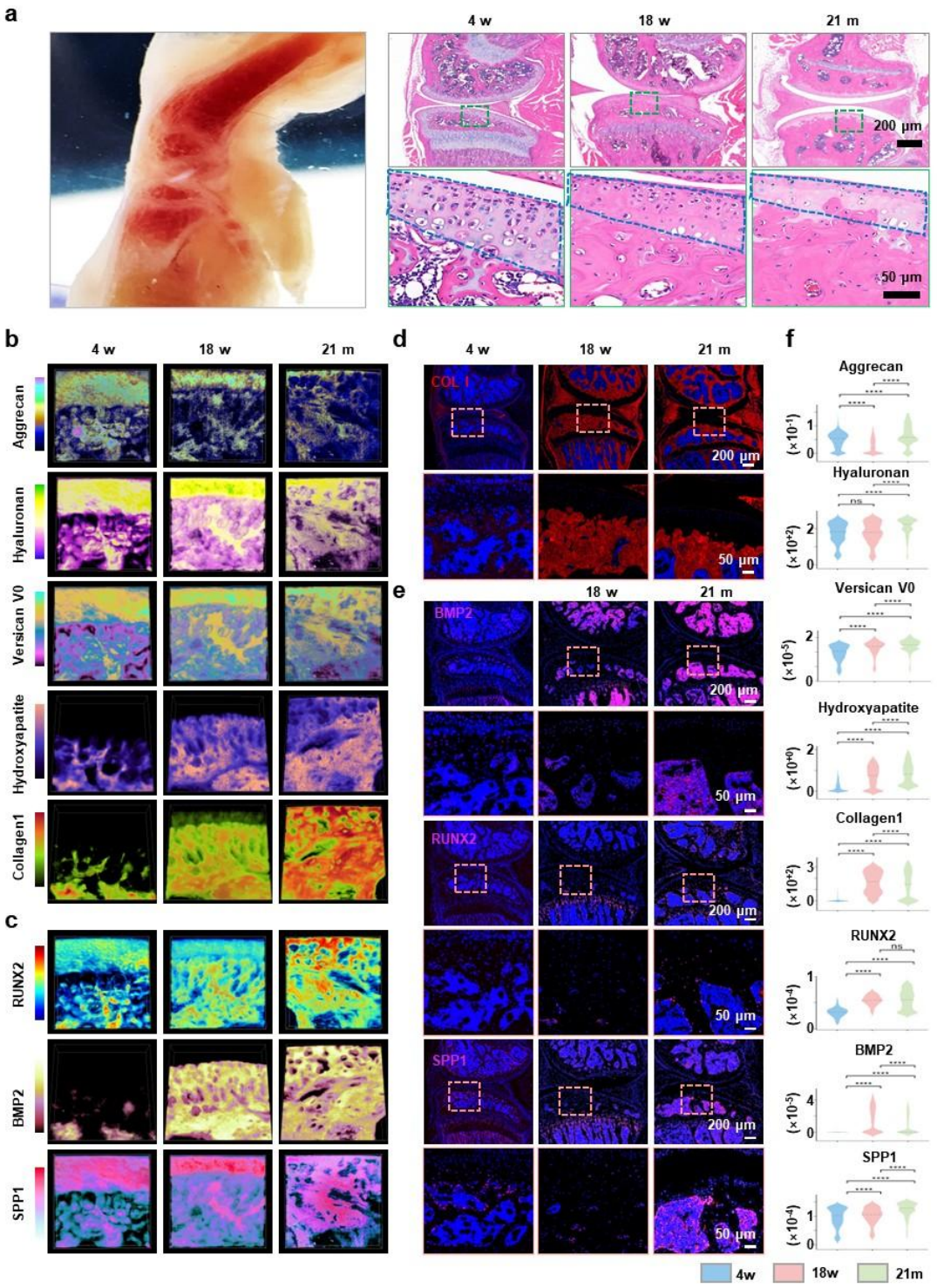

a
4 w
18 w
21 m
200 μm
50 μm
b
4 w
18 w
21 m
Aggrecan
Hyaluronan
Versican V0
Hydroxyapatite
Collagen1
c
RUNX2
BMP2
SPP1
d
4 w
18 w
21 m
COL I
200 μm
50 μm
e
18 w
21 m
BMP2
RUNX2
SPP1
f
Aggrecan
Hyaluronan
Versican V0
Hydroxyapatite
Collagen1
RUNX2
BMP2
SPP1
4w
18w
21m

Fig. 3

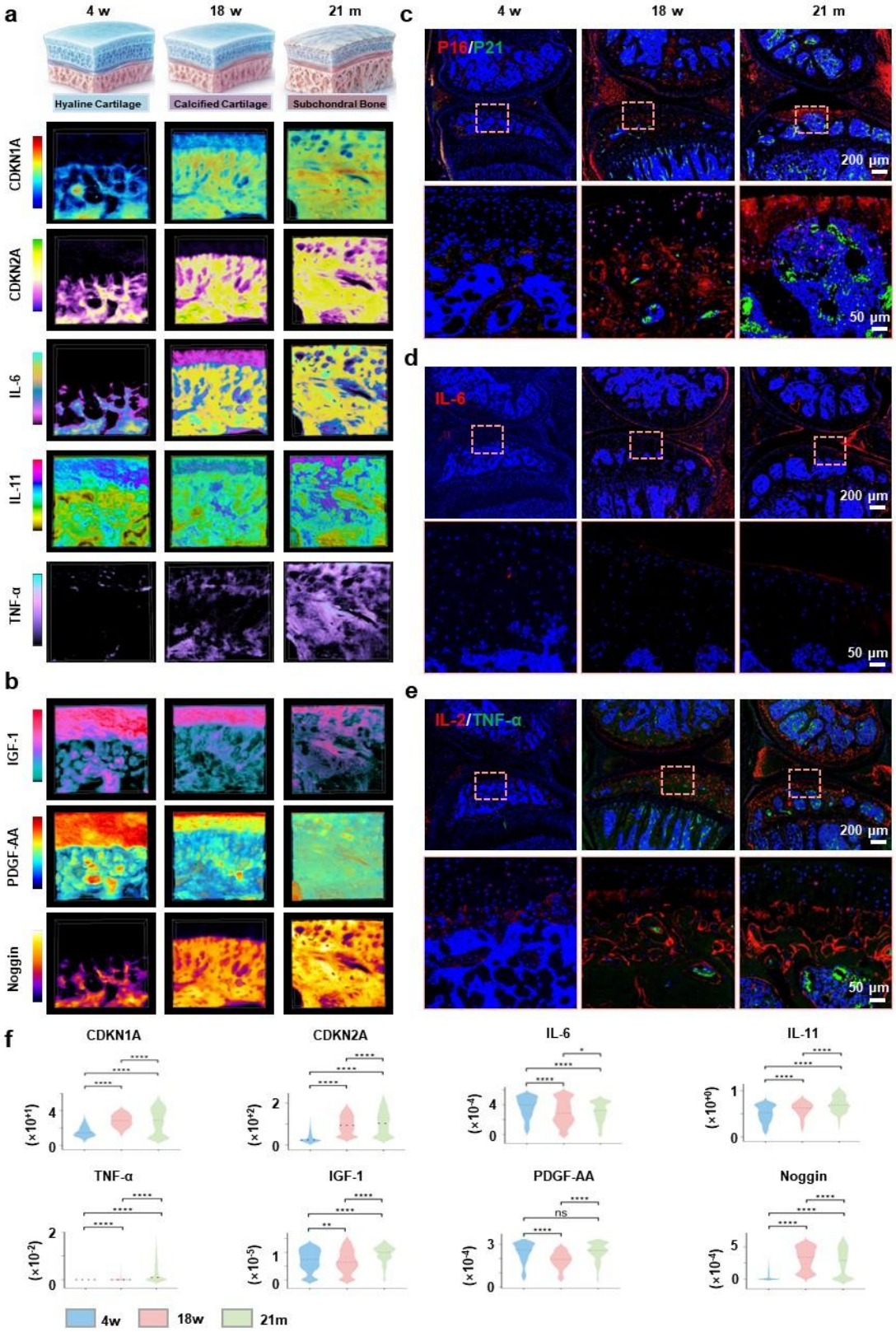

a
4 w
18 w
21 m
Hyaline Cartilage
Calcified Cartilage
Subchondral Bone
CDKN1A
CDKN2A
IL-6
IL-11
TNF-α
b
IGF-1
PDGF-AA
Noggin
c
4 w
18 w
21 m
P16/P21
200 μm
50 μm
d
IL-6
200 μm
50 μm
e
IL-2/TNF-α
200 μm
50 μm
f
CDKN1A
CDKN2A
IL-6
IL-11
TNF-α
IGF-1
PDGF-AA
Noggin
ns
4w
18w
21m

Fig. 4

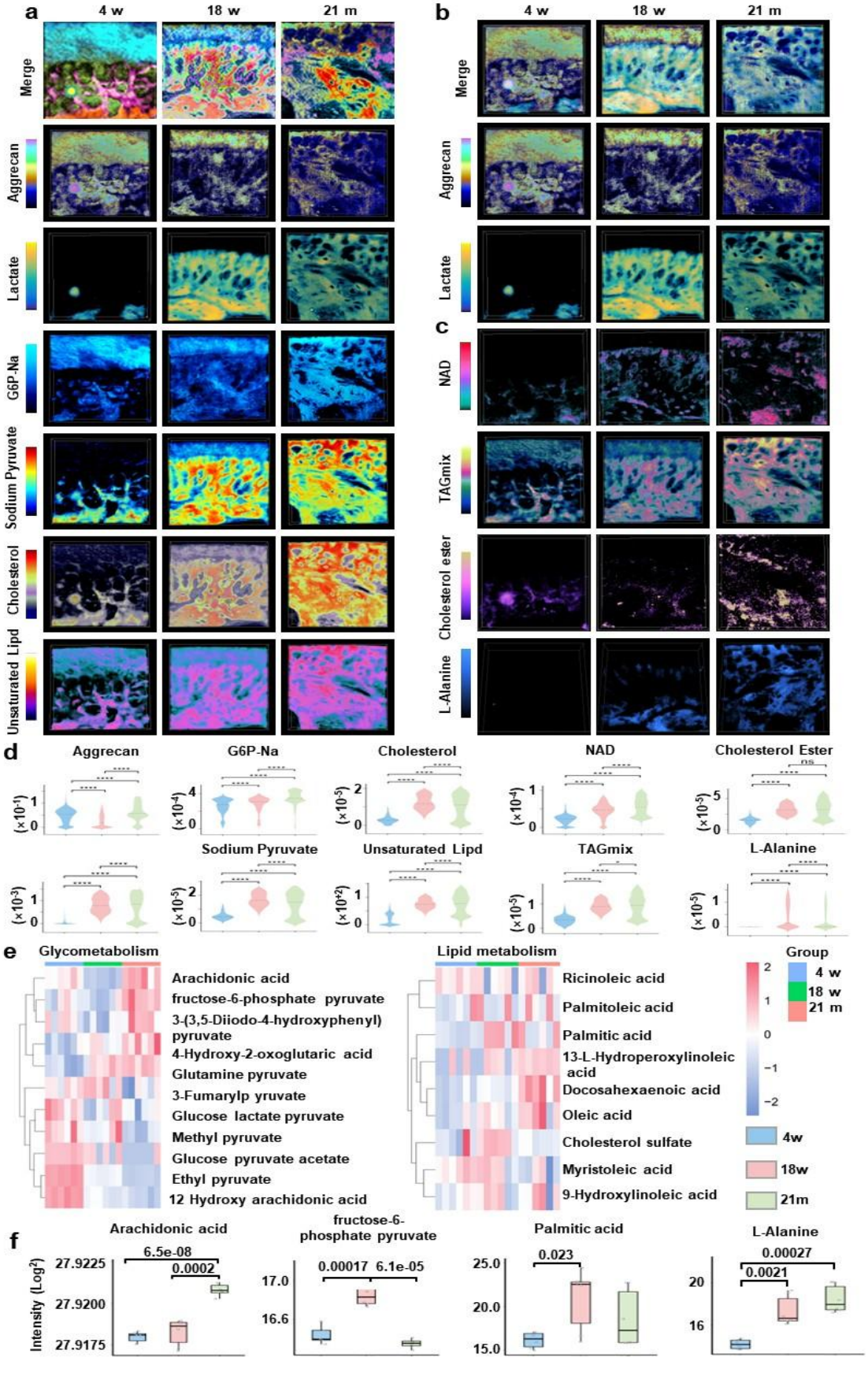
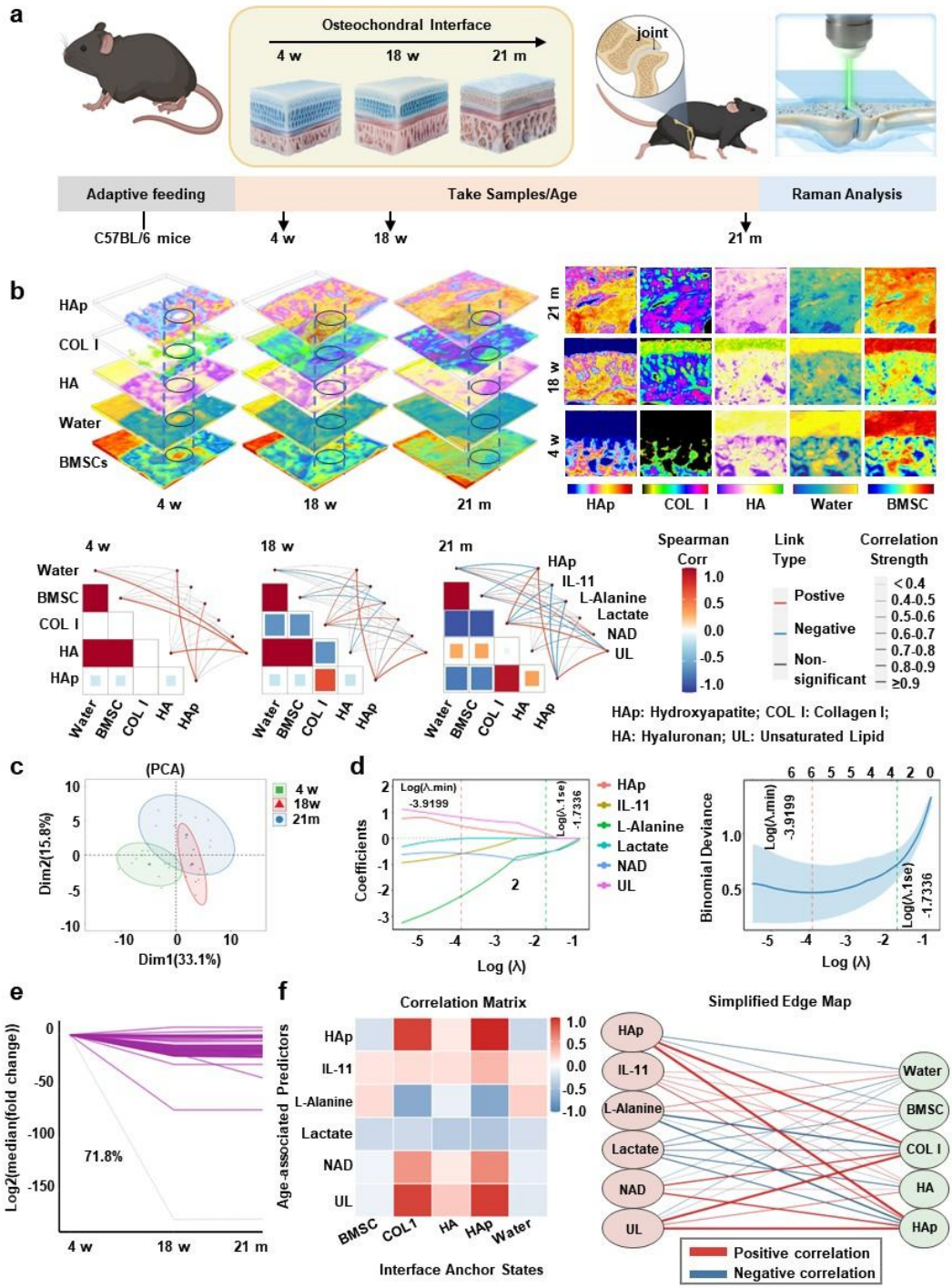

a
4 w
18 w
21 m
Merge
Aggrecan
Lactate
G6P-Na
Sodium Pyruvate
Cholesterol
Unsaturated Lipd
b
Merge
Aggrecan
Lactate
c
NAD
TAGmix
Cholesterol ester
L-Alanine
d
Aggrecan
G6P-Na
Cholesterol
NAD
Cholesterol Ester
Sodium Pyruvate
Unsaturated Lipd
TAGmix
L-Alanine
ns
e
Glycometabolism
Arachidonic acid
fructose-6-phosphate pyruvate
3-(3,5-Diiodo-4-hydroxyphenyl) pyruvate
4-Hydroxy-2-oxoglutaric acid
Glutamine pyruvate
3-Fumarylp yruvate
Glucose lactate pyruvate
Methyl pyruvate
Glucose pyruvate acetate
Ethyl pyruvate
12 Hydroxy arachidonic acid
Lipid metabolism
Ricinoleic acid
Palmitoleic acid
Palmitic acid
13-L-Hydroperoxylinoleic acid
Docosahexaenoic acid
Oleic acid
Cholesterol sulfate
Myristoleic acid
9-Hydroxylinoleic acid
Group
4 w
18 w
21 m
4w
18w
21m
f
Arachidonic acid
6.5e-08
0.0002
Intensity (Log2)
fructose-6-phosphate pyruvate
0.00017
6.1e-05
Palmitic acid
0.023
L-Alanine
0.00027
0.0021

Fig. 5


a
Osteochondral Interface
4 w
18 w
21 m
joint
Adaptive feeding
Take Samples/Age
Raman Analysis
C57BL/6 mice
4 w
18 w
21 m
b
HAp
COL I
HA
Water
BMSCs
4 w
18 w
21 m
HAp
COL I
HA
Water
BMSC
Spearman Corr
1.0
0.5
0.0
-0.5
-1.0
Link Type
Postive
Negative
Non-significant
Correlation Strength
< 0.4
0.4-0.5
0.5-0.6
0.6-0.7
0.7-0.8
0.8-0.9
≥0.9
IL-11
L-Alanine
Lactate
NAD
UL
HAp: Hydroxyapatite; COL I: Collagen I;
HA: Hyaluronan; UL: Unsaturated Lipid
c
(PCA)
4 w
18w
21m
Dim2(15.8%)
Dim1(33.1%)
d
Log(λ.min)
-3.9199
Log(λ.1se)
-1.7336
Coefficients
Log (λ)
Binomial Deviance
e
Log2(median(fold change))
71.8%
f
Correlation Matrix
Age-associated Predictors
Interface Anchor States
Simplified Edge Map
Positive correlation
Negative correlation

Supplementary Files

This is a list of supplementary files associated with this preprint. Click to download.

- SupplementaryInformation1.docx
- Reportingsummary.pdf